A new cascade-regularized spatial encoding technique using non-linear field disturbance of susceptibility markers

Hirad Karimi[1], William Dominguez-Viqueira[2], and Charles H. Cunningham[1,2]

[1]*Dept. of Medical Biophysics, University of Toronto, Toronto, Ontario, Canada,* [2]*Imaging Research, Sunnybrook Research Institue, Toronto, Ontario, Canada*

Introduction: Conventional linear gradient fields generated using gradient coils usually perform spatial encoding in MRI. These coils are stationary relative to any physiological movements and this ultimately limits the spatial resolution. Some applications such as intravascular MR imaging (iMRI) could benefit from the high-resolution images that could result from new approaches [1]. Here, a new encoding technique that allows encoding fields to move with physiological structures is investigated. The method uses only the field perturbations emanating from markers with different susceptibilities as the encoding fields [2] (The gradient coils on scanner are not used). Fig. 1 shows the scaled-up device prototype (3cm diameter) and its associated field perturbations. Simulations and phantom studies were conducted to further validate the result.

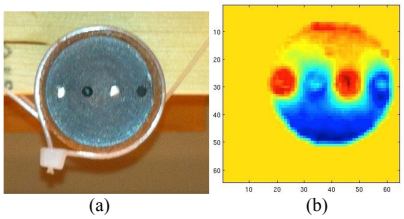

(a) (b)

Fig. 1: (a) Markers configuration. Black markers are graphite and silver markers are titanium (b) field perturbations due to markers ranging form -400Hz(blue) to 200Hz(red)

Theory: Paramagnetic and diamagnetic markers perturb magnetic fields in their vicinity once they exposed to a magnetic field [3]. Fig. 1b shows these field perturbations as a result of linear configuration of markers. The non-homogeneous magnetic fields are then used for spatial-encoding of signals. The resultant magnetic field perturbations are moved as we rotate the device by a certain degree (θ^0). By rotating the device for 360^0, sufficient information can be acquired to reconstruct a forward-view image of a phantom at the tip of the device. Eq. 1 shows the encoding matrix (E). In this equation, we assumed to have M × N discrete voxels and perform acquisition for K angles and record FIDs for read-out time equal to t_L. In reality signal values at each timepoint will be summation of all signals from a continuous medium as shown in Eq. 2a. Elements of the encoding matrix have been computed using the field perturbations and prescribed acquisition parameters as described. Due to the fact that spatial encoding is a linear process, the reconstructed image pixel values, arranged as a vector (ρ), can be computed by solving a set of over-determined linear equations as shown in Eq. 2, or equivalently by computing decoding matrix (F) as shown in Eq. 3 where s is the signal vector. If the spatial encoding fields were linear, solving Eq. 2b would be equivalent to perform Fourier transform on the signals (conventional 2DFT). Because of non-linearity nature of encoding fields, there is not a one-to-one relationship between acquired signals and spatial frequencies. The encoding matrix in Eq. 1 is usually ill-conditioned. Taking the pseudo-inverse of the encoding matrix will result in a poor reconstruction. A cascade regularization technique was used to reduce the ill-posedness of the encoding matrix and improve the accuracy of reconstruction process with Truncated Singular Value Decomposition (TSVD) followed by Tikhonov regularization. Fig. 2 depicts the flowchart of the proposed technique for computing the decoding matrix (F) using the encoding matrix (E). Spatial Response Functions (SRFs) are used to characterize spatial distributions of a discrete voxel that is shown in Fig. 3. SRFs are computed using linear combination of phase maps generated by the device for different timepoint as shown in Eq. 4. In this equation, $\boldsymbol{enc}\,(\theta_i, \tau_j)$ is the 2D phase map at angle θ_i, time τ_j and $F\,(\rho_k, \theta_i, \tau_j)$ is one of the decoding matrix (F) rows corresponding to voxel (ρ_k).

Fig. 2: Cascade regularization flowchart

Fig. 3: (a) SRF for a voxel (b) SRF for center voxel

$$E = \begin{bmatrix} e^{-i\omega_1(x_1,y_1)t_1} & \cdots & e^{-i\omega_1(x_M,y_N)t_1} \\ \vdots & \ddots & \vdots \\ e^{-i\omega_K(x_1,y_1)t_L} & \cdots & e^{-i\omega_K(x_M,y_N)t_L} \end{bmatrix} \quad \text{Eq. 1}$$

$$s(t) = \iint \rho(x,y) e^{-i\omega(x,y)t}\, dx\, dy \;\; (a), \qquad \tilde{s} = E\tilde{\rho} \;\; (b) \quad \text{Eq. 2}$$

$$\tilde{\rho} = F\tilde{s} \quad \text{Eq. 3}$$

$$\mathrm{SRF}(\rho_k) = \sum_i \sum_j F\,(\rho_k, \theta_i, \tau_j)\boldsymbol{enc}\,(\theta_i, \tau_j) \quad \text{Eq. 4}$$

Methods: In order to compute the true field perturbations of the device and minimize shifts induced by the inhomogeneous fields, we used hard pulse excitation and pulsed phase-encoding in both X and Y directions (i.e. a single k-space position per TR). FIDs were recorded and two consecutive samples of each FID were assigned to two distinct K-spaces. This is somewhat equivalent to acquiring two GRE images with same acquisition parameters except for echo-time (TE). We acquired the field perturbation using described pulse sequence (TR=25ms, FOV=40cm, BW=19.23KHz, FA=90, 64 phase-encodes for each direction) for two echo times equal to 400μs and 500μs. Fig. 1b depicts the field perturbation for the condition of the device as shown in Fig. 1a. Frequency shifts due to markers vary from -400Hz to 200Hz. Signals encoded by the device were acquired using a pulse sequence consisting of a 250μs hard pulse and a 20ms sampling window (the conventional gradients were not used) every 8^0 angle steps. The data acquired with TE=300μs, FA=90, FOV=3cm, BW=10KHz, 2048 samples in read-out direction and TR=6s to allow manual rotation of the device.

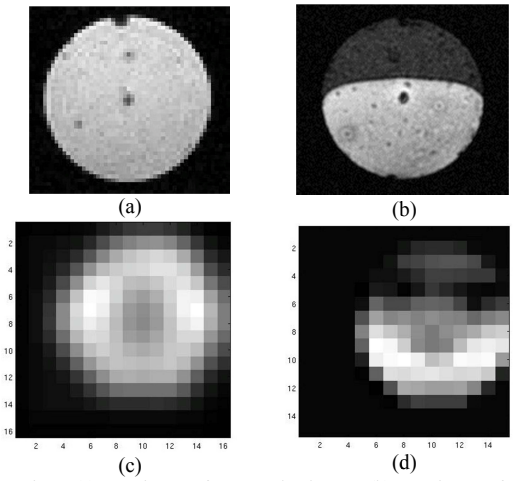

(a) (b) (c) (d)

Fig. 4: (a) GRE image of water-only phantom (b) GRE image of water-oil phantom (c) Reconstructed image of water-only phantom 16×16 voxels (d) Reconstructed image of water-oil phantom 16×16 voxels

Results and Discussion: To validate the technique, we built two phantoms, one completely filled with water and one partly filled with oil and water as shown in Fig. 4a and Fig. 4b respectively (GRE, TE=4.9ms, TR=17ms, FA=60, 128x128). Reconstructed images, using real signals that are encoded with the device, are shown in Fig. 4c and Fig. 4d. The same decoding matrix F is used to reconstruct both images, which have FOV 3cm and spatial resolution of 2mm. The regions of different contrast in Fig. 4d correlate well (qualitatively) with the oil and water regions seen in Fig. 4c. An artifact, visible as a hypointense region, is visible at the center of both (c) and (d). This agrees with Fig. 3b, where the SRF for the center point is lower in amplitude and not as confined as the SRF shown in Fig. 3a for an off-center point. Therefore it will degrade the reconstruction accuracy for center points as shown in Fig. 4 (c) and (d). Considering new marker configurations could make correction for this artifact.

Conclusion: A novel encoding technique was previously proposed [1] and extended in this work. Here, we introduced a new reconstruction technique as well as a new configuration of susceptibility markers that reduced the duplication artifact previously observed and improved the reconstruction accuracy. Same decoding matrix has been used for both phantoms that shows the new technique works for general cases. In future work, we aim to build a catheter-sized encoding device to perform phantom and *ex vivo* studies for further validation of the new encoding technique.

Acknowledgments: We would like to acknowledge Canadian Institute of Health Research (CIHR) for funding this project.

References: [1] Sathyanarayana and Bottomley, Med. Phys. 36 P. 908 2009 [2] Karimi H. and Cunningham C.H. ISMRM 5296, 2011 [3] Schenck J. *et al*, Med. Phys. 23, 1996